nature materials

SUPPLEMENTARY INFORMATION

https://doi.org/10.1038/s41563-018-0211-5

In the format provided by the authors and unedited.

Magneto-ionic control of magnetism using a solid-state proton pump

Aik Jun Tan[1], Mantao Huang[1], Can Onur Avci[1], Felix Büttner[1,2], Maxwell Mann[1], Wen Hu[2], Claudio Mazzoli[2], Stuart Wilkins[2], Harry L. Tuller[1] and Geoffrey S. D. Beach[1]*

[1]Department of Materials Science and Engineering, Massachusetts Institute of Technology, Cambridge, MA, USA. [2]National Synchrotron Light Source II, Brookhaven National Laboratory, Upton, NY, USA. *e-mail: gbeach@mit.edu

- Supplementary Information -

Magneto-ionic control of magnetism using a solid-state proton pump

Aik Jun Tan, Mantao Huang, Can Onur Avci, Felix Büttner, Maxwell Mann, Wen Hu, Claudio Mazzoli, Stuart Wilkins, Harry L. Tuller, Geoffrey S.D. Beach

I. Rate of voltage-induced Co redox under different atmospheric conditions

Figure 1 in the main text shows anomalous Hall effect measurements of the out-of-plane hysteresis loops for CoO and Co films when gate bias has been applied in various atmospheres for 1000s. Figure S1 shows time-dependent data corresponding to those measurements. Figure S1a (S1b) shows the rate of change in out-of-plane magnetization probed using anomalous Hall effect (AHE) as a positive (negative) V_G is applied to a Pt/CoO/GdO_x (Pt/Co/GdO_x) Hall cross device under different atmospheric conditions (t_{GdOx} = 30nm). The reduction of CoO to Co at V_G = +3V (Fig. S1a) occurs at a very similar rate in ambient and in wet N_2, whereas no discernable reduction of CoO is observed in vacuum and dry O_2. At T= 25ºC and humidity level of > 90%, we have P_{H2O} ~ 20mbar in this experiment. Under similar conditions, Shirpour[1] *et al.* observed a two orders of magnitude increase of proton conductivity in Gd-doped CeO_2 compared to dry conditions (P_{H2O} ~ 0mbar). A similar enhancement in proton conductivity is also observed in Y-doped ZrO_2[2]. Our results are very consistent with these findings[1–3]. Similarly, for the oxidation of Co to CoO (Fig. S1b), we observe a very similar rate of oxidation in ambient and in wet N_2 indicating a dominant proton transport process[4–9]. However, in this case, Co is also oxidized under dry O_2, indicating that there is a parallel oxidation process based on oxygen ion transport [10–12]. This process is likely slower due to higher activation energy for ionic transport through oxygen vacancies [1–3,11,12].

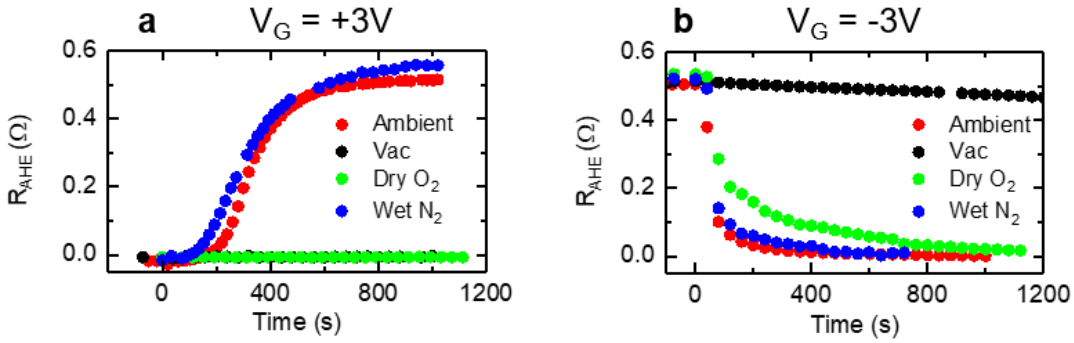

Figure S1| Effect of V_G in different atmospheric conditions. a, Anomalous Hall effect resistance R_{AHE} vs time at V_G = +3V applied to a CoO structure. **b,** R_{AHE} vs time at V_G = -3V applied to a Co structure.

II. Effect of electrode thickness on rate of voltage-induced reduction of CoO to Co

Figures S2a shows the transient magneto-optical Kerr effect (MOKE) magnetization remanence ratio, M_r/M_s at the center of a device with structure Pt(3nm)/CoO(0.9nm)/GdO_x (20nm)/Au (t =3,4,6,10 nm) as V_G = +3V is applied. We observe that the hydrogen insertion induced magnetization change becomes slower with increasing thickness of Au, indicating that hydrogen is sourced from H_2O in ambient during the reduction process. The reduction activity is highest at the electrode edge where the thickness of Au is thinner due to shadowing effect from shadow mask lithography. This can be seen in the optical micrograph in Figure S2b for a t = 4nm Au electrode. The bottom plot in Figure S2b shows a snapshot of M_r/M_s across the electrode after V_G = +3V for ~600s. One can see that CoO is reduced to Co by H injection at the edges (Fig. S2c). With increasing bias dwell time, this region of modified properties moves inward towards the center. Figure S2d shows the transient (V_G = +3V) for a t = 6nm Au electrode at the edge vs the

center, where a relatively constant M_r/M_s followed by a sharp increase further indicates a circular "front" of changed properties that is slowly moving inward from the edge towards the center.

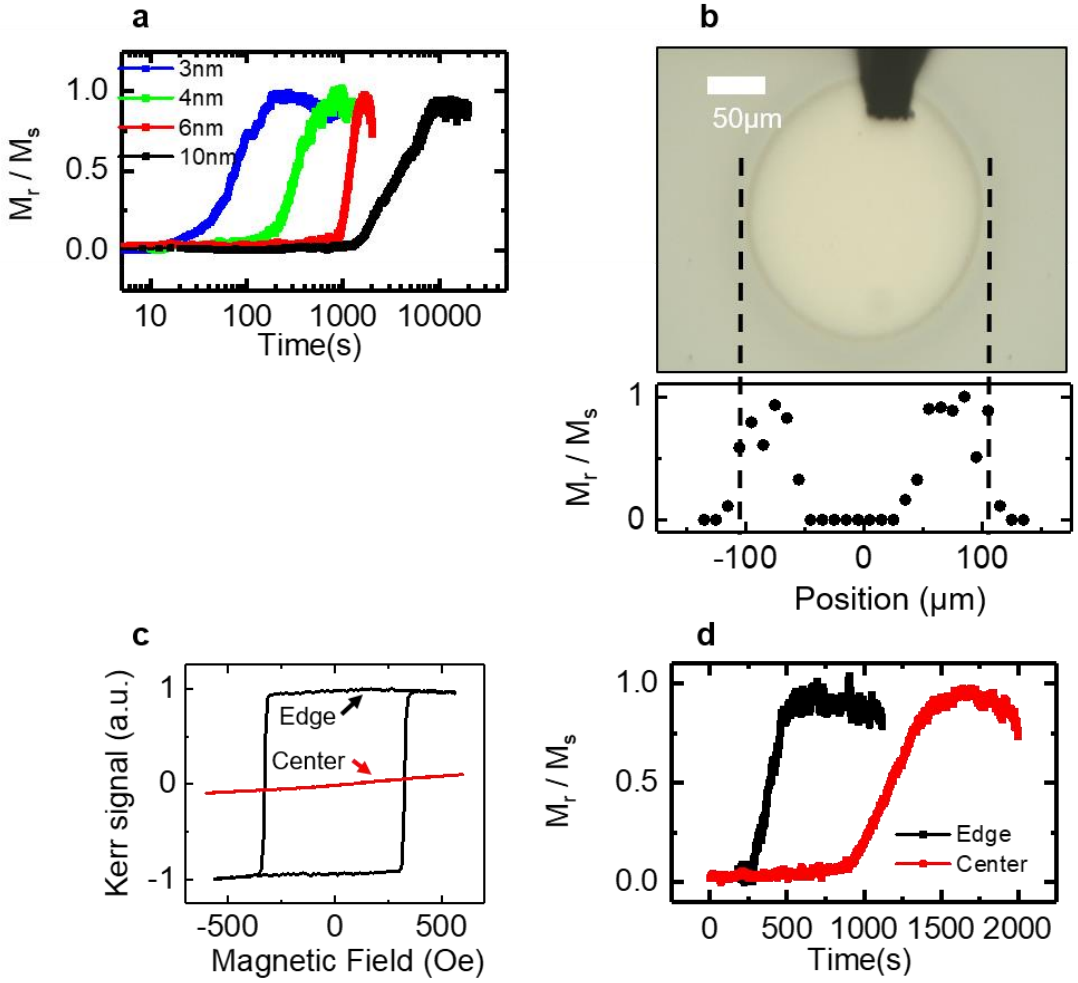

Figure S2| Voltage-driven injection of hydrogen at edge of electrode. a, Magneto-optical Kerr effect (MOKE) magnetization remanence ratio, M_r/M_s versus time as V_G =+3V is applied to a Pt(3nm)/CoO(0.9nm)/GdO_x (20nm)/Au (t nm) device. **b,** Top: Optical micrograph of a t = 4nm electrode. Bottom: Snapshot of M_r/M_s across the electrode at ~600s. **c,** Hysteresis loops corresponding to center and edge of electrode in **b** at ~600s. **d,** Magnetization transient for t = 6nm electrode at the edge vs the center.

III. Proton conductivity enabled by water dissolution

Many of the best proton conductors, such as $BaZrO_3$ and $BaCeO_3$, are doped with lower valent yttrium substituting on the Zr or Ce sublattice to generate high concentrations of oxygen vacancies[8]. This, in turn, enables high levels of water dissolution into solid solution via the following mechanism written in Kroger-Vink defect notation[13]

$$H_2O + O_O^x + V_O^{\cdot\cdot} \rightarrow 2OH_O^{\cdot} \quad (1)$$

where O_O^x represents an oxygen ion on a normal oxygen site, $V_O^{\cdot\cdot}$ an oxygen vacancy with net double positive charge relative to the normally occupied lattice site and $OH_O^{\cdot}$ a singly positively charged proton localized around an oxygen ion sitting on a normal oxygen site. These protons are found to diffuse readily in the aforementioned perovskites and other well-known oxygen deficient oxides including for example TiO_{2-x}[9].

To test the importance of water incorporation in the GdO_x layer for our structures, we compared the difference in magneto-ionic response between a Pt(3nm)/Co(0.9nm)/GdO_x (4nm)/Ta(1.4nm)/Au(5nm) devices prepared under two conditions, i) with the top electrode deposited in-situ under vacuum using a shadow mask, without vacuum break; and ii) with the top electrode deposited after first exposing the top GdO_x layer to ambient atmosphere for 2 weeks. Remarkably, as seen in Figure S3a, when the electrode is deposited without first exposing GdO_x to atmosphere, no magneto-ionic effects are achieved under positive bias. By contrast, for the sample in which the electrode was deposited after vacuum break (Fig. S3b), magneto-ionic switching under positive bias is observed. It is reasonable to anticipate a significant amount of water uptake from this ambient environment, given the hygroscopic character of GdO_x[7]. In this case, $OH_O^{\cdot}$ is expected to be incorporated in the oxide which should enhance proton transport, just

as we observe experimentally. The evidence that oxygen vacancies exist in Gd_2O_3 to allow for creation of $OH_O^{\cdot}$ sites can be seen from the fact that voltage-induced oxidation of Co is also observed in dry O_2 (Fig. 1l of the main text) due to oxygen ion transport through oxygen vacancies[11–13].

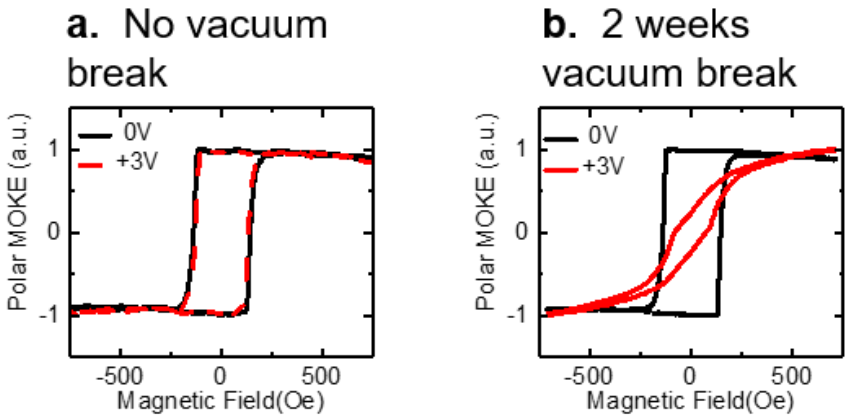

Figure S3| Effect of exposure of GdO_x layer to ambient moisture on magneto-ionic response of a Pt/Co/GdO_x device. a, Polar magneto-optical Kerr effect (MOKE) hysteresis loops of Pt/Co/GdO_x device at V_G = 0V and +3V with no vacuum break between deposition of the GdO_x layer and the Ta/Au top electrode. **b,** Polar MOKE hysteresis loops of Pt/Co/GdO_x device at V_G = 0V and +3V with 2 weeks of vacuum break between deposition of the GdO_x layer and the Ta/Au top electrode.

IV. Cyclic voltammetry of Pt/GdO_x/Au device

Figures S4a-b show cyclic voltammetry (CV) data for a Pt(3nm)/GdO_x(20nm)/Au(3nm) structure under different atmospheric conditions (Fig. S4a) and at different sweep rates (Fig. S4b). Note that the Co layer is not present in this structure. We assume that the top Au electrode acts as the working electrode while the bottom Pt electrode acts as the counter/reference electrode[14]. When cyclic

voltammetry is performed under different atmospheres (Fig. S4a), significant anodic and cathodic currents are observed only when H_2O is present. Both currents are governed by the voltage sweep rate (v) (Fig S4b) which indicates a process that is kinetically limited by mass transport rather than charge-transfer[14]. From both information, we can conclude that water hydrolysis ($V_G > 0$) and recombination ($V_G < 0$) are indeed taking place[15–17]. Despite the lack of a unique reference electrode, the classical exponential behavior observed in oxidation is consistent with oxygen evolution reaction (OER) while the peak observed in reduction is typical of oxygen reduction reaction (ORR)[18].

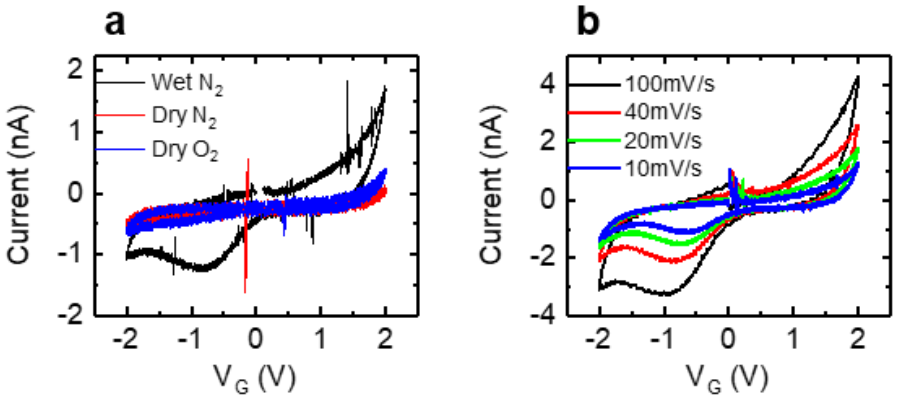

Figure S4| Dependence of overall reaction rate on charge transfer and mass transport. a, Cyclic Voltammetry (CV) plot under different atmospheric conditions performed at v = 10mV/s.**b,** CV plot at different sweep rates performed in ambient.

V. Device retention

Figure S5 shows polar magneto-optical Kerr effect (MOKE) hysteresis loops of a Pt(3nm)/Co(0.9nm)/GdO_x(30nm) device in the virgin state (a), after V_G = +3V is applied for 5min in ambient (b), after the device is then left at open circuit for 80 hours in ambient (c), and after V_G

= =-0.5V is applied to recover the PMA in ambient (d). A small reverse bias is applied here instead of simply short-circuiting the device in order to speed up the recovery of PMA. We observe that the in-plane state can be retained for at least 3 days at open circuit indicating excellent retention of the stored hydrogen. We emphasize that hydrogen removal requires electron transport from the bottom electrode to the top electrode so that Eqs. 3,4 in the main text can occur in reverse. Hence, the long-term stability of the hydrogen-loaded in-plane state under open circuit depends on the electronic leakage current through the GdO_x, which provides an alternate path for electrons from the bottom electrode to the top electrode. To demonstrate the correlation between hydrogen retention and leakage current across GdO_x, we also measured retention time as a function of device resistance (Figure S5i). The retention time is defined as the duration it takes for the magnetization to relax back to an out-of-plane state at open circuit after it rotates in-plane under V_G = +3V. The device resistance, which directly gauges the leakage current across the oxide, is measured at V_G = +3V after it has been applied for 5min. From the data, we can clearly see that retention depends crucially on the leakage current; the smaller the leakage, the longer the retention. A small leakage minimizes the transfer of electrons which can lead to removal of the hydrogen (Eq. 3 and 4 in reverse).

In ambient, even in high-resistance devices, albeit slow, there is still a gradual relaxation of the magnetization back to an out-of-plane state indicating some loss of the hydrogen due to a finite leakage current. Another way to prolong the retention of hydrogen is to remove any oxygen which can recombine with the stored hydrogen. We find that the hysteresis loops show no detectable change after even >1 week when the device is set to a hydrogen loaded state and then placed in vacuum, since Eq. 3 in the main text cannot proceed (in reverse). We demonstrate this by first applying V_G = +3V to load hydrogen into the device (Figure S5f). We then attempt to remove the

hydrogen by applying a small reverse bias (V_G = -0.5V) in vacuum (~ 10^{-4}mbarr). From the results (Figure S5g), we can clearly see that the device remains in a hydrogen-loaded state due to the absence of oxygen, even when electronic current can flow. As mentioned, Eq. 3 in the main text cannot occur (in reverse), so the removal of hydrogen from the bottom electrode cannot proceed. However, when we next place the device in ambient (Figure S5h), we can see that the magnetization returns to the out-of-plane state when electronic current flows, indicating removal of the hydrogen through recombination with oxygen. This result shows that hydrogen cannot simply diffuse away from the bottom electrode. Rather, first the neutral H must split into a proton and an electron, and the proton is transported through the GdO_x while the electron is transported to the top electrode via an external circuit or internal leakage path. Only then, can the top electrode reaction proceed, following the anodic and cathodic reverse reactions shown in Eq. 3,4 of the main text.

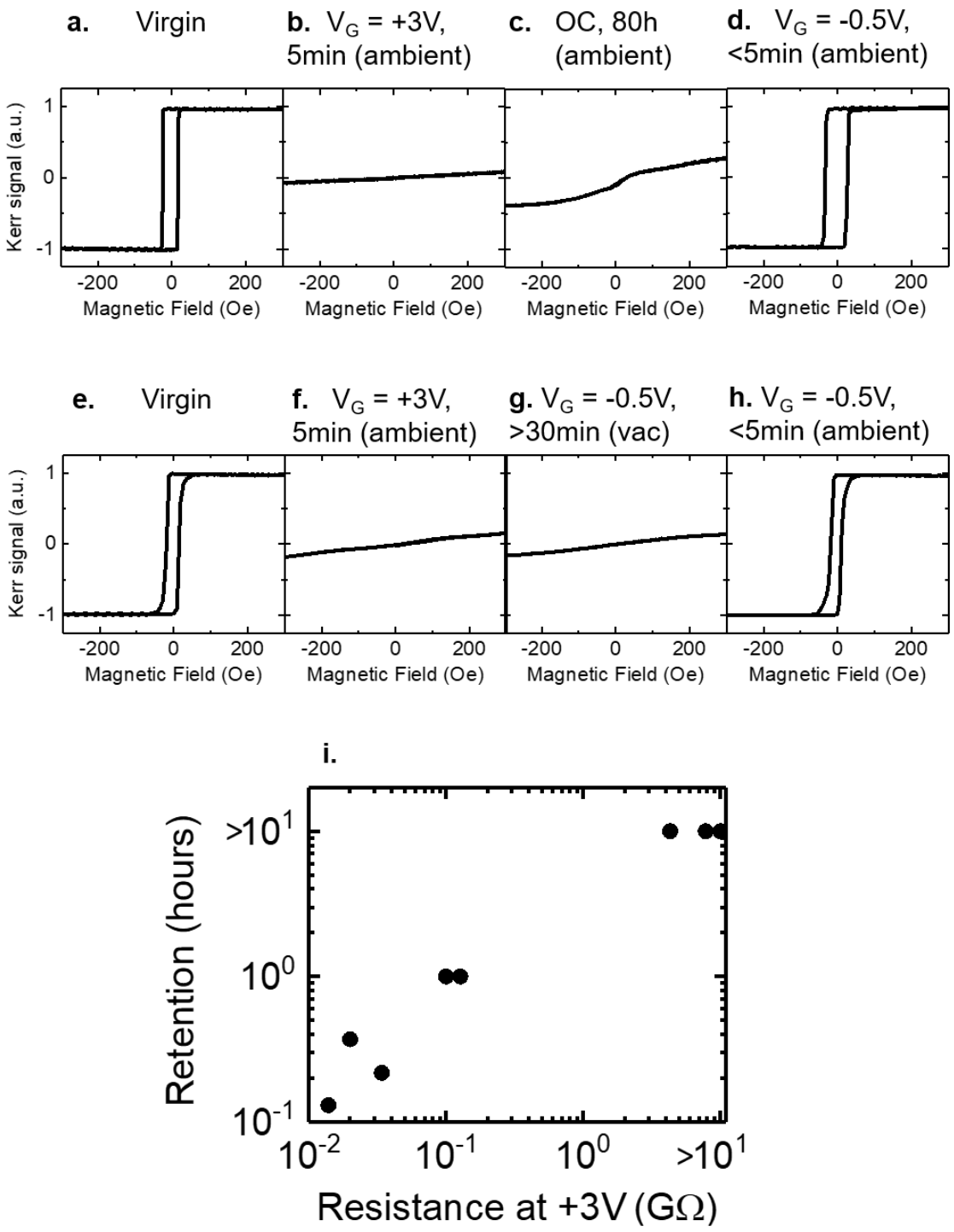

Figure S5| Device retention at open circuit. a-d, Polar magneto-optical Kerr effect (MOKE) hysteresis loops of a Pt/Co/GdO_x device in virgin state (a), after V_G = +3V is applied for 5min in ambient (b), after the device is set to open-circuit for 80 hours in ambient(c), and after applying a

small reverse bias(V_G = -0.5V) in ambient. **e-h,** Similar experiments as in **a-d** but after hydrogen loading, the device is placed in vacuum (~10^{-4}mbarr), where it is seen that a reverse bias does not allow recovery of the PMA state. However, when the device is returned to an ambient environment, a small reverse bias quickly brings the magnetization back out of plane, indicating removal of hydrogen. **i,** Retention as a function of device resistance. The retention time is defined as the duration it takes for the magnetization to relax back to an out-of-plane state at open circuit after it rotates in-plane under V_G = +3V

VI. Recombination of stored hydrogen for spontaneous recovery of PMA

Figures S6 shows the magneto-optical Kerr effect (MOKE) magnetization remanence ratio, M_r/M_s versus time at short-circuit after V_G =+3V is applied to a Pt(3nm)/ Co(0.9nm)/GdO_x (10nm)/Au (3 nm). The graph also displays the discharge current that accompanies the change in magnetization. Immediately after applying the positive bias and injecting hydrogen, as per Eqs. 3,4 in the main text, the device exhibits an open circuit voltage of ~1.2V. As per Eqs. 3,4, this does not arise from charge imbalance, but rather represents the chemical potential (Nernst potential), which tends to drive the reaction in reverse. Once the device is set to closed circuit, reactions given by Eqs. 3,4 in the main text proceed in reverse, leading to a measurable current flow, as shown in Fig. S6. Note that this discharge current flows in the **opposite** direction relative to the current at V_G = +3V, indicating recombination of stored hydrogen. Integration of the discharge current in the first 5 seconds shows that removal of ~40nC or 4.1 x 10^{-13} mol of hydrogen leads to full recovery of PMA. This corresponds to ~1H for every 10 Co atoms assuming Co density of 8.9g/cc and molar mass of 58.9g/mol. Note that this ratio represents an upper bound to the amount of hydrogen needed to toggle the magnetization between in-plane and out-of-plane

state. The actual value can be much smaller since some of the hydrogen may be stored in the GdO_x is not immediately adjacent to the Co/GdO_x interface.

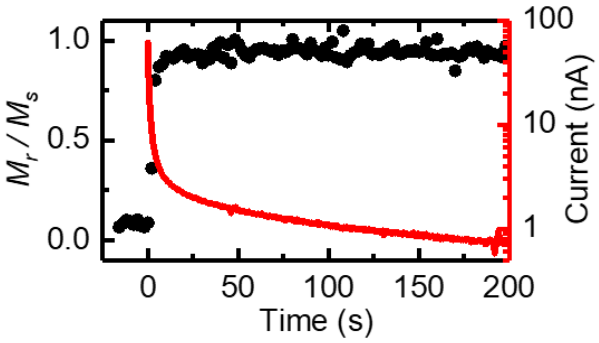

Figure S6| Recombination of stored hydrogen during recovery of PMA. Magneto-optical Kerr effect magnetization remanence ratio (M_r/M_s) and discharge current versus time at V_G = 0V after V_G =+3V is applied to a Pt(3nm)/ Co(0.9nm)/GdO_x (10nm)/Au (3 nm). Note that this discharge current flows in the **opposite** direction relative to the current at V_G = +3V

VII. Effect of humidity on magneto-ionic switching based on hydrogen accumulation at Co/GdO_x interface

Figure S7a-b show the rate of change in out-of-plane and in-plane magnetization probed using the anomalous Hall effect (AHE) and planar Hall effect (PHE) as V_G = +3V is applied to a Pt/Co/GdO_x Hall cross device under different atmospheric conditions (t_{GdOx} = 30nm). The data clearly indicates that the magnetization rotates from out-of-plane to in-plane only in the presence of moisture, implying that H_2O in the environment acts as the source of hydrogen[19,20] which is accumulated at the Co/GdO_x interface[21]. Figures S7c-e show the corresponding AHE hysteresis loops in the virgin state (Fig. S7c) and after V_G = +3V is applied for 800s in vacuum (Fig. S7d) and wet N_2 (Fig. S7e). Figures S7f-h show the corresponding PHE hysteresis loops.

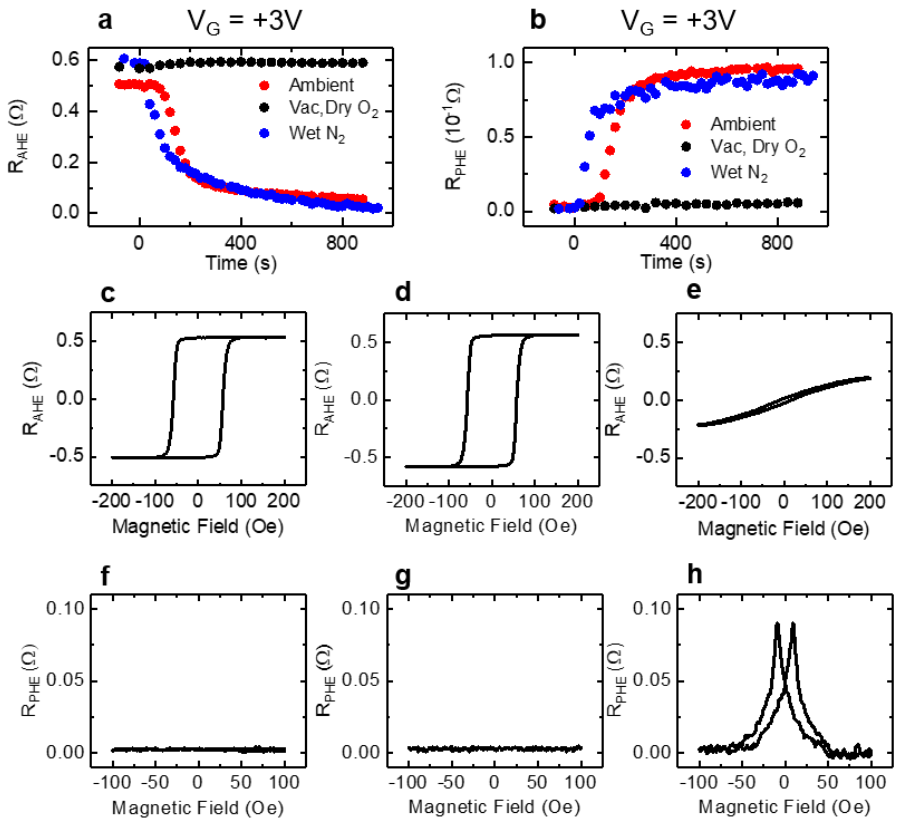

Figure S7| Effect of positive V_G in different atmospheric conditions starting from a Co virgin state. a, Anomalous Hall effect resistance (R_{AHE}) vs time at V_G = +3V. **b,** Planar Hall resistance (R_{PHE}) vs time at V_G = +3V. **c-e,** AHE hysteresis loops of the device in virgin state (**c**), and after V_G = +3V is applied for 800s in vacuum (**d**)and in wet N_2 (**e**) . **f-h,** PHE hysteresis loops of the device corresponding to the condition in **c-e** respectively.

VIII. Voltage-induced reduction of CoO to Co followed by hydrogen accumulation at the Co/GdO_x interface

Figures S8a-b show the out-of-plane and in-plane magnetization probed using anomalous Hall effect (AHE) and planar hall effect (PHE), respectively, as V_G = +3V is applied to a Pt/CoO/GdO_x (t_{GdOx} = 30nm) structure. In its virgin state, the CoO layer is nonmagnetic. When a positive gate bias is applied, CoO is reduced to Co and we start to observe an increase in out-of-plane

magnetization (R_{AHE}) which eventually plateaus as all the CoO is reduced [22,23]. During this period, we do not observe any in-plane magnetization (R_{PHE}). However, as the voltage is applied for longer, the magnetization eventually rotates in plane due to accumulation of hydrogen at the Co/GdO_x interface[21].

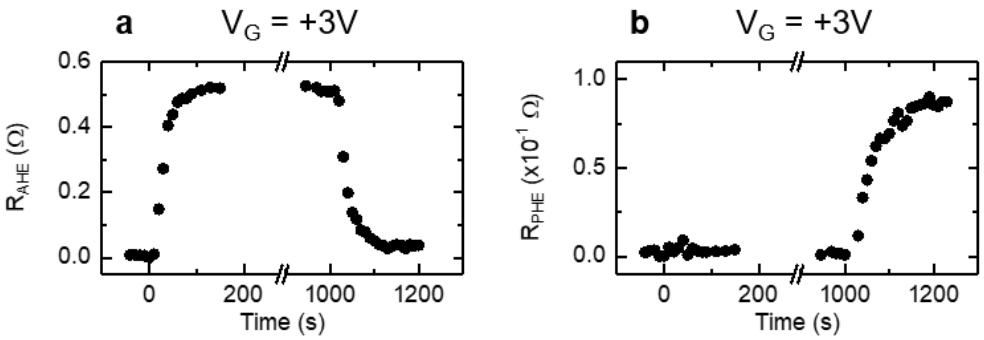

Figure S8| Evolution of magnetization under a prolonged positive V_G on CoO virgin device. **a,** Anomalous Hall effect resistance (R_{AHE}) vs time at V_G = +3V. **b,** Planar Hall effect resistance (R_{PHE}) vs time at V_G = +3V.

IX. Irreversible oxidation of Co during negative V_G

In the main text we state that hydrogen-mediated magneto-ionic switching allows for better cyclability than Co redox-based magnetoionic switching that has been widely reported in the literature. Exemplary results for voltage driven oxidation and reduction of Co using positive/negative gate voltage cycles are shown in Figure S9. Figure S9a shows the remanent magnetization ratio (M_r/M_s)for a $Pt/Co/GdO_x$ device with t_{GdOx} = 4nm as V_G is cycled between +2V and -2V at 0.1Hz. M_r/M_s values are obtained from polar magneto-optical Kerr effect (MOKE) hysteresis loops at 170ms intervals. Figure S9b shows the hysteresis loop at the end of the application of V_G = +2V for cycle 1 and cycle 12. The data clearly show degradation of

PMA with time as the Co layer gets increasingly oxidized. This irreversibility likely arises from uneven oxidation of the Co grains. As a result, when a positive V_G is applied, some regions of the Co film are reduced while others are shielded from the electric field[24].

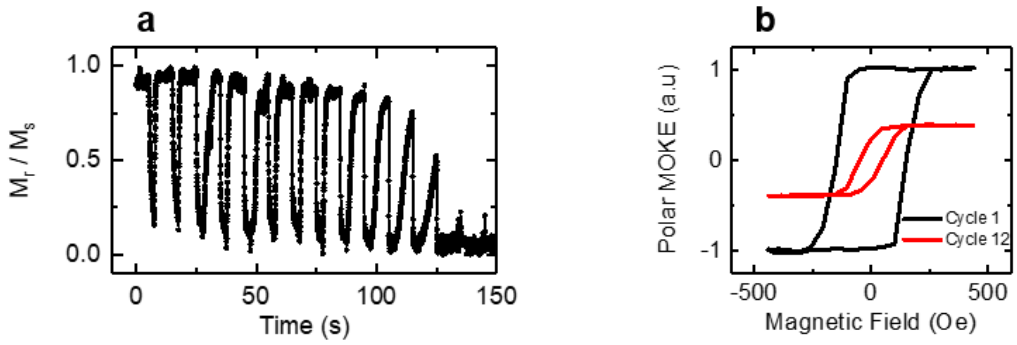

Figure S9| Magneto-ionic switching based on Co redox. a, Switching cycles of M_r/M_s using square wave V_G between +2V and -2V at 0.1Hz. **b**, Polar magneto-optical Kerr effect (MOKE) hysteresis loops at V_G = +2V for cycle 1 and cycle 12 of switching in (**a**).

X. Speed of 90º magnetization switching based on hydrogen accumulation at Co/GdO_x interface.

Figures S10a-b show the change in polar magneto-optical Kerr effect (MOKE) magnetization remanence ratio, M_r/M_s at the rising and falling edge of V_G, respectively, for a Pt (3nm)/Co (0.9nm)/GdO_x (4nm) device obtained from 25ms polar MOKE hysteresis loops.

The switching times at the two edges are ~100ms and ~400ms.

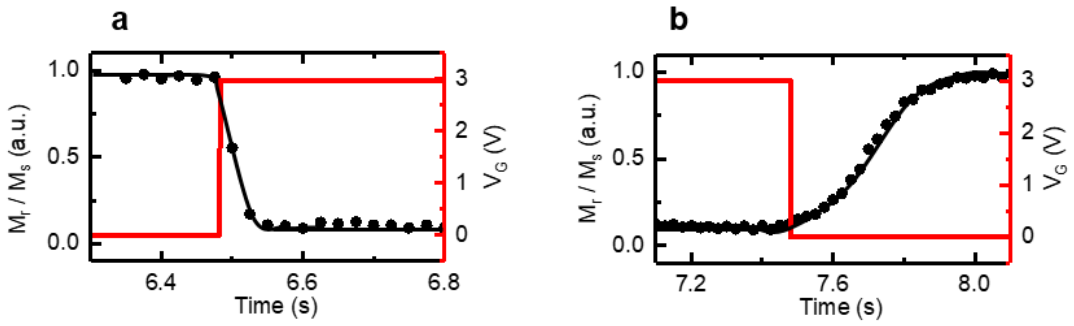

Figure S10| Magneto-ionic switching speed of a Pt/Co/GdO$_x$ structure. a-b, Polar magneto-optical Kerr effect magnetization remanence ratio M_r/M_s at rising (**a**) and falling edge (**b**) of V_G.

XI. Speed of 90º magnetization switching based on hydrogen loading in Pd adjacent to a Co magnetic layer.

Figures S11a- b show the change in in polar magneto-optical Kerr effect (MOKE) magnetization remanence ratio, M_r/M_s at the rising and falling edge of V_G respectively for a Pd (3nm)/Co(0.6nm)/Pd(4.5nm)/GdO$_x$ (10nm) device obtained from 25ms polar MOKE hysteresis loops. The switching time is ~150ms at both edges.

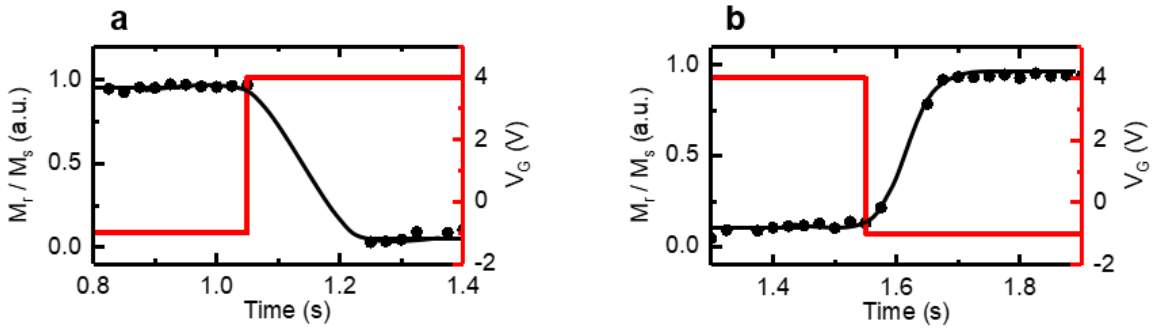

Figure S11| Magneto-ionic switching speed of a Pd/Co/Pd/GdO_x structure. a-b, Polar magneto-optical Kerr effect magnetization remanence ratio M_r/M_s at rising (**a**) and falling edge (**b**) of V_G.

XII. X-ray absorption spectra (XAS) of GdO_x and Pd/GdO_x thin films

Figures S12 compares the X-ray absorption spectra for GdO_x (30nm) and Ta(4nm)/Pd(6nm)/GdO_x (30nm) on Si substrates. There is clearly a peak at 532eV for the latter sample, while only a 'shoulder' is observed for the GdO_x film. This confirms that the observed peak at ~532eV is indeed the Pd M_3 peak[25].

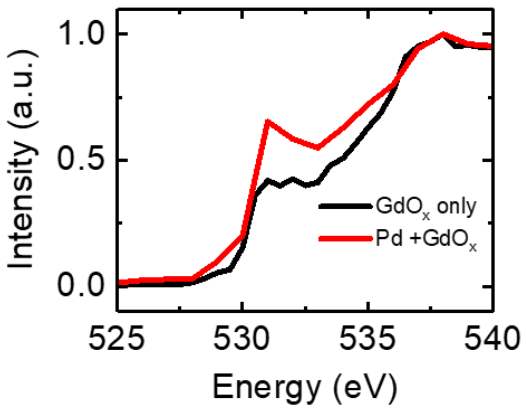

Figure S12| X-ray absorption spectra of GdO_x (black) and Pd/GdO_x (red) thin film samples on Si substrates.

XIII. X-ray absorption spectra (XAS) of Mg K-edge for a Mg/Pd/GdO_x/Au device

Figure S13 shows the X-ray absorption spectra of Mg K-edge for a Ti(3nm)/Mg(40nm)/Pd(5nm)/GdO_x (30nm)/Au(3nm) device in the virgin state and after a

positive bias is applied to the top electrode in ambient (V_G =+3V, for 5 minutes). In this structure, Mg acts as the hydrogen loading layer while Pd acts as the protective layer to prevent Mg oxidation. Comparison of the XAS data of the biased device and the literature data[26] shows that the Mg layer becomes hydrided upon application of a positive gate bias, V_G = +3V. We should note that before such a thick Mg (40nm) can be loaded with hydrogen, the entire Pd layer will have to be penetrated by hydrogen. Such a substantial amount of hydrogen loaded into the system is far more than what would be required to explain the magnetic property changes observed in the thin film structures in our experiments.

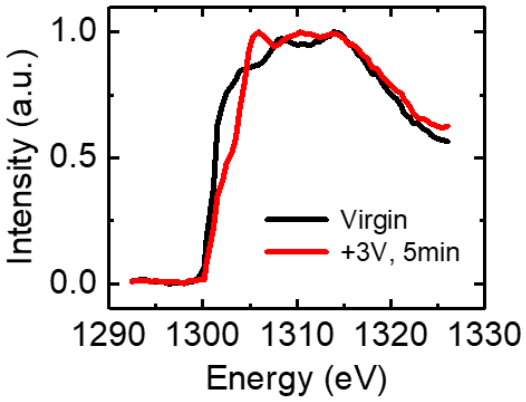

Figure S13| X-ray absorption spectra of Mg K-edge. Mg K-edge of a Ti(3nm)/Mg (40nm)/Pd (5nm)/GdO_x (30nm)/Au(3nm) structure in virgin state (black) and after V_G = +3V is applied for 5min (red). Mg K-edge of the biased device shows remarkable similarity to that of MgH_x[26].

XIV. Magnetic Anisotropy Energy

Figures S14a shows out-of-plane hysteresis loop probed through the anomalous Hall effect resistance (R_{AHE}) for a Pt(3nm)/ Co(0.9nm)/ GdO_x (30nm) structure while figure S14b shows R_{AHE} as a function of in-plane field, H_x applied along the current injection line for the virgin state. The

red curve shows a fit to the single-domain Stoner-Wohlfarth model, $R_{AHE} = R_{sat} \cos(\arcsin(H_x/H_K))$ in order to obtain the in-plane saturation field, H_K. R_{sat} is the AHE resistance when the magnetization is saturated in the out-of-plane direction. The fitted H_K is ~8.2kOe, and assuming M_s of 1400emu/cc for Co, the uniaxial magnetic anisotropy, $K_u = (H_k M_s)/2$ is 5.7×10^6 erg/cc. Normalizing by the thickness of the Co layer, t_{Co} (0.9nm), we obtain interfacial magnetic anisotropy, $K_s = t_{Co} (H_k M_s)/2$ of 0.52erg/cm^2. This value represents the lower limit for the change in K_s when the magnetization rotates from out-of-plane to in-plane under $V_G > 0$. With an electric field of 1MV/cm (V_G = +3V) , this corresponds to a magnetoelectric efficiency of > 5200fJ/ Vm.

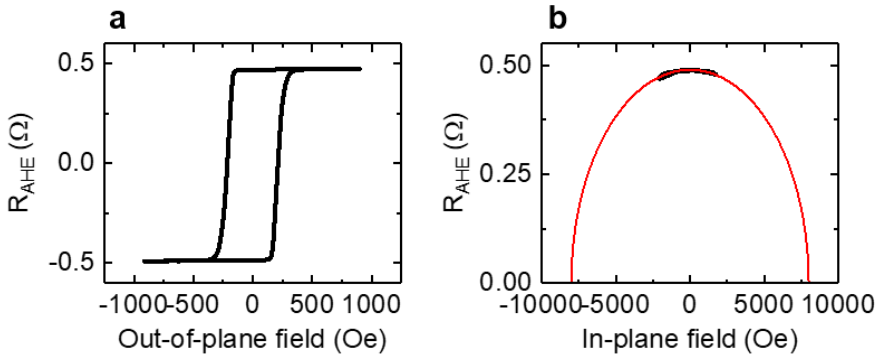

Figure S14| Quantification of magnetic anisotropy energy. a, Out-of-plane hysteresis loop probed through the AHE resistance (R_{AHE}) for a Pt(3nm)/ Co(0.9nm)/ GdO_x (30nm) structure. **b,** R_{AHE} as a function of in-plane magnetic field. The red line shows the fit for a single domain Stoner-Wohlfarth model.

References

1. Shirpour, M., Gregori, G., Merkle, R. & Maier, J. On the proton conductivity in pure and gadolinium doped nanocrystalline cerium oxide. *Phys. Chem. Chem. Phys.* **13,** 937–940

(2011).

2. Scherrer, B. *et al.* On proton conductivity in porous and dense yttria stabilized zirconia at low temperature. *Adv. Funct. Mater.* **23,** 1957–1964 (2013).

3. Avila-Paredes, H. J. *et al.* Grain boundaries in dense nanocrystalline ceria ceramics: exclusive pathways for proton conduction at room temperature. *J. Mater. Chem.* **20,** 10110 (2010).

4. Kreuer, K. Proton Conductivity : Materials and Applications. *Chem.Mater* **8,** 610–641 (1996).

5. Norby, T., Widerøe, M., Glöckner, R. & Larring, Y. Hydrogen in oxides †. *Dalt. Trans.* 3012–3018 (2004).

6. Larring, Y. & Norby, T. Protons in rare earth oxides. *Solid State Ionics* **77,** 147–151 (1995).

7. Adachi, G. & Imanaka, N. The Binary Rare Earth Oxides. *Chem. Rev.* **98,** 1479–1514 (1998).

8. Bi, L., Boulfrad, S. & Traversa, E. Steam electrolysis by solid oxide electrolysis cells (SOECs) with proton-conducting oxides. *Chem. Soc. Rev.* **43,** 8255–8270 (2014).

9. Erdal, S. *et al.* Hydration of Rutile TiO_2 : Thermodynamics and Effects on n- and p-Type Electronic Conduction. *J. Phys. Chem. C* **114,** 9139–9145 (2010).

10. Skinner, S. J. & Kilner, J. A. Oxygen ion conductors. *Mater. Today* **6,** 30–37 (2003).

11. Subbarao, E. C. & Maiti, H. S. Solid Electrolytes with Oxygen Ion Conduction. *Solid State Ionics* **11,** 317–338 (1984).

12. Tuller, H. L. Ionic conduction in nanocrystalline materials. *Solid State Ionics* **131,** 143–157 (2000).

13. Tuller, H. L. & Bishop, S. R. Point Defects in Oxides: Tailoring Materials Through Defect Engineering. *Annu. Rev. Mater. Res.* **41,** 369–398 (2011).

14. Bard, A. J., Faulkner, L. R., Swain, E. & Robey, C. *Electrochemical Methods: Fundamentals and Applications*. (John Wiley and Sons).

15. Rossmeisl, J., Logadottir, A. & Nørskov, J. K. Electrolysis of water on (oxidized) metal surfaces. *Chem. Phys.* **319,** 178–184 (2005).

16. Rossmeisl, J., Qu, Z., Zhu, H., Kroes, G. & Norskov, J. K. Electrolysis of Water on Oxide Surfaces. *J. Electrochem. Chem.* **607,** 83–89 (2007).

17. Nørskov, J. K. *et al.* Origin of the Overpotential for Oxygen Reduction at a Fuel-Cell Cathode. 17886–17892 (2004).

18. Stamenkovic, V. R., Strmcnik, D., Lopes, P. P. & Markovic, N. M. Energy and Fuels from Electrochemical Interfaces. *Nat. Mater.* **16,** 57–69 (2017).

19. Sander, D. *et al.* Reversible H-induced switching of the magnetic easy axis in Ni/Cu(001) thin films. *Phys. Rev. Lett.* **93,** 247203 (2004).

20. Yin, Q. *et al.* Cathode bubbles induced by moisture electrolysis in TiO_{2-x}-based resistive switching cells. *J. Phys. D. Appl. Phys.* **49,** 09LT01 (2016).

21. Yoon, H. *et al.* Reversible phase modulation and hydrogen storage in multivalent VO_2 epitaxial thin films. *Nat. Mater.* **15,** 1113–1119 (2016).

22. Manchon, a *et al.* X-ray analysis of the magnetic influence of oxygen in $Pt/Co/AlO_x$

trilayers. *J. Appl. Phys.* **103,** 07A912-3 (2008).

23. Manchon, A. *et al.* Analysis of oxygen induced anisotropy crossover in Pt / Co / MOx trilayers. *J. Appl. Phys.* **104,** 43914 (2008).

24. Gilbert, D. A. *et al.* Structural and magnetic depth profiles of magneto-ionic heterostructures beyond the interface limit. *Nat. Commun.* **7,** 12264 (2016).

25. Thompson, A. C. & D.Vaughn. *X-RAY DATA BOOKLET*. (2001).

26. Richardson, T. J. *et al.* X-ray absorption spectroscopy of transition metal-magnesium hydride thin films. *J. Alloys Compd.* **356–357,** 204–207 (2003).